ACS Partner Journal
PRECISION CHEMISTRY

pubs.acs.org/PrecisionChem
Article

Reversible Interlayer Coupling/Decoupling in Bilayer Graphene Regulated by Electrochemical Hydrogenation

Yanbo Zhang,[‖] Yizhe Wang,[‖] Wenchang Zhang, Na Shu, Xiaolan Wang, Yan Yu, Kun Ni,* and Yanwu Zhu*

Cite This: https://doi.org/10.1021/prechem.5c00315
Read Online

ACCESS | Metrics & More | Article Recommendations | Supporting Information

ABSTRACT: Chemical functionalization can effectively regulate the properties of graphene by altering π electrons, but the direct control of interlayer interaction in bilayer graphene (BLG) by such a technique remains elusive. Herein, we report an *in situ* observation of reversible interlayer coupling/decoupling in BLG, which is sensitive to electrochemical hydrogenation. It is found that electrochemical potential applied via an organic electrolyte containing protons causes preferential hydrogenation of one graphene layer in BLG, accompanied by the presence of new Raman modes. At the same time, the other graphene layer remains almost intact under electrochemical gating, resulting in an overall high electric conductance yet sensitive to the interlayer decoupling in BLG. With density functional theory simulations, 4H-BLG is identified as a critical intermediate structure during hydrogenation, and the van der Waals interaction in BLG is effectively modified by sp^3 bonding formed on the hydrogenated layer. Our work provides new insights into the regulation of interlayer interaction through surface functionalization in van der Waals stacking materials.

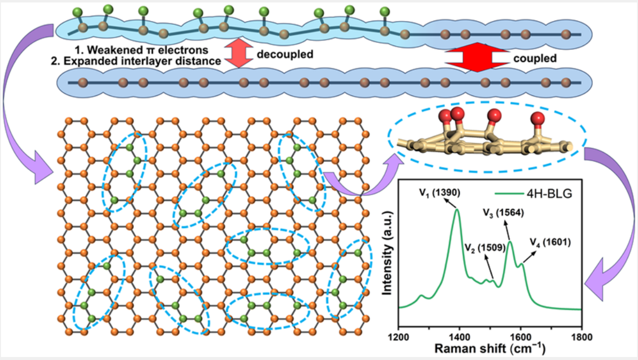

KEYWORDS: *bilayer graphene, chemical functionalization, electrochemical hydrogenation, interlayer coupling, in situ Raman spectroscopy*

INTRODUCTION

As Herbert Kroemer stated that "the interface is the device",[1] the entanglement between multiple degrees of freedom including orbitals, charges, spins, and lattice at the interface strongly modulates the electronic structure and properties, leading to the appearance of exotic interfacial phenomena that are not found in their bulk counterparts, *e.g.*, fractional quantum Hall effect,[2] interface superconductivity,[3] and magnetoelectric coupling.[4] The interfacial effect in two-dimensional (2D) materials is more pronounced, as a large fraction or even all of the atoms are exposed to interfacial interactions.

As a basic model of 2D materials, graphene provides an open and atomically precise interface for the subtle modification on the surface[5,6] to further extend the functions that are not demonstrated in graphite. By regulation of the interface between graphene and substrate, a band gap can be generated and tuned in graphene. For example, the formation of C—O—Al bonding on the graphene/sapphire interface breaks the sublattice symmetry of graphene and thus opens up a small energy gap.[7] The creation of covalent C—Si bonding between graphene and silicon carbide has achieved a band gap of 0.6 eV and a mobility of ~5000 $cm^2\ V^{-1}\ S^{-1}$ at room temperature in graphene.[8] In addition, the surface of graphene can be adjusted by both in-plane doping and out-of-plane chemical functionalization. For instance, heteroatom doping of graphitic nitrogen on the surface can create strong polarization and ferromagnetism in graphene.[9] The adsorption of hydrogen atoms[10] or extended molecular network[11] changes the hybridization from sp^2 to sp^3, leading to a significant change of the lattice and electronic structure of graphene.

In addition to the modifications at the surface of graphene, as listed above, the relatively weak van der Waals (vdW) interlayer interaction can influence the electronic and optical properties of graphene stackings as well. A prominent example is that, for the bilayer graphene (BLG) with a twisting angle $\theta \approx 1.1°$, the band structure near the Fermi level becomes flat, leading to the appearance of unconventionally strong electron correlations, such as quantum anomalous Hall effects,[12] topological insulator states,[13] and unconventional superconductivity.[14] By applying high pressures, the vdW interaction in BLG can be further enhanced, leading to ultrafast energy relaxation of hot carriers via a new relaxation pathway related

Received: November 17, 2025
Revised: January 14, 2026
Accepted: January 19, 2026

ACS Publications

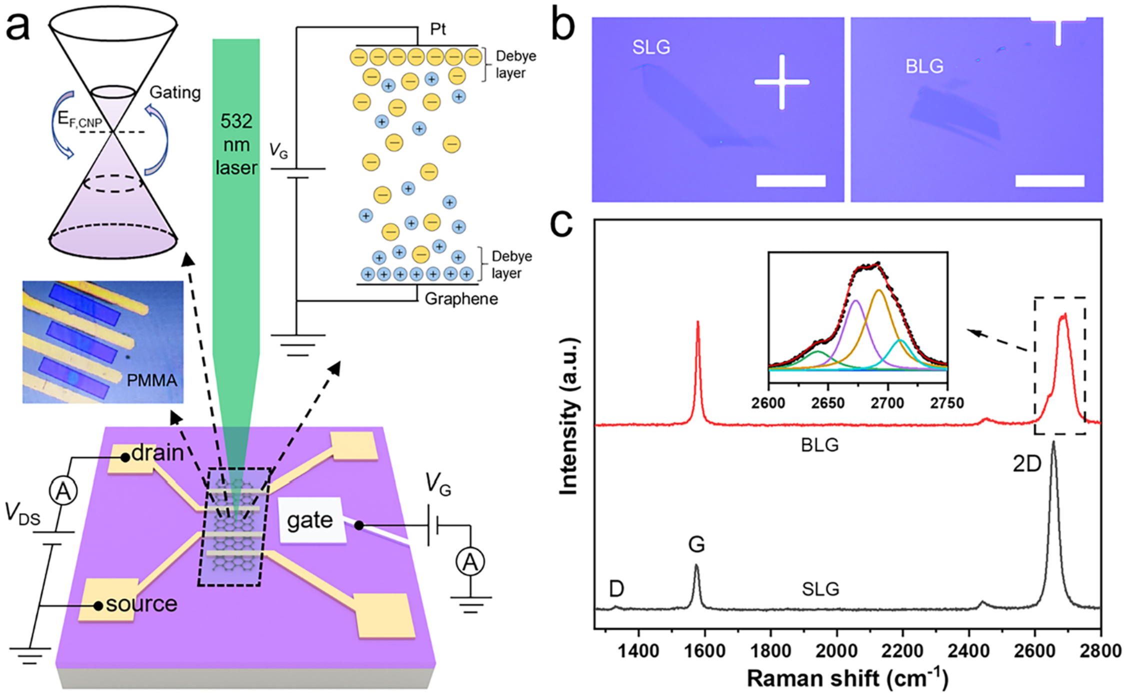

Figure 1. Device configuration and identification of graphene layers. (a) Schematic illustration of the electrochemical hydrogenation device. (b) Typical optical microscope images of exfoliated graphene flakes. left: SLG, right: BLG. Scale bars: 50 μm. (c) Raman spectra of SLG and BLG on SiO_2/Si. The inset shows the 2D peak of BLG deconvoluted with Lorentzian peaks.

to the interlayer phonon modes.[15] On the contrary, the intercalation of guest molecules like $FeCl_3$ into BLG can expand the interlayer distance from 3.35 to 9.37 Å, resulting in complete decoupling of graphene layers, evidenced by the upshift of G peak and a Lorentzian shape of 2D band in Raman spectroscopy, and the elimination of excitonic transition between the van Hove singularities.[16,17]

Clearly, the regulation of either the surface or interface can modify the property of graphene. Comparatively, little attention has been paid to the correlation between the surface structure and interlayer coupling in graphene stacking. Recently, Son et al. found that the double-side fluoridated BLG is insulating, while the single-side fluorinated BLG remains conductive, indicating an electrical decoupling between the intact layer and the fluorinated layer.[18] Another study shows that the BLG functionalized by a diazonium salt exhibits a weakened interlayer coupling, while the in-plane nitrogen doping leads to an enhanced interlayer coupling, as evidenced by the changes of surface potential measured by scanning Kelvin probe microscopy.[19] On the other hand, it was reported that the electrochemical hydrogenation can achieve a reversible adsorption of H atoms on BLG, resulting in a conductor−insulator transition and a large electronic gap opening.[20] Such an electrochemical gate-controlled hydrogenation provides an approach to hydrogen storage with a capacity of ∼6.6 wt % by Pt-catalyzed electroreduction of protons in an electrolyte.[21] Despite the progresses described above, the detailed process on how surface hydrogenation influences the interlayer coupling of BLG remains elusive.

Herein, we demonstrate that electrochemical hydrogenation can simultaneously modify the surface of BLG and the interlayer interaction in BLG, which exhibits a hydrogenation-dependent, reversible coupling, and decoupling of layers. By employing *in situ* Raman spectroscopy and density functional theory (DFT) calculations, we reveal a preferential chemisorption of proton (H^+) on one layer of BLG in an organic H^+ electrolyte under bias. Under high potentials, the formation of localized hydrogenation structures activates new Raman modes between 1400 and 1530 cm^{-1}, related to the vibration of distorted carbon rings. The measurement of electrical conductivity demonstrates that the deteriorated conjugation of π-electrons in the hydrogenated layer causes a significantly weakened interlayer coupling, leaving the other layer electrically conductive, like intrinsic single-layer graphene (SLG).

RESULTS AND DISCUSSION

Electrochemically Gated Field-Effect Transistor of Graphene

To effectively control the hydrogenation of graphene and simultaneously monitor the changes of electrical properties, an electrochemically gated field-effect transistor (FET) device was fabricated, as shown in Figure 1a. In our experiment, graphene flakes were mechanically exfoliated from natural graphite and then transferred onto SiO_2/Si substrates. SLG and BLG flakes were identified by optical contrast (Figure 1b)[22] and Raman spectroscopy (Figure 1c). Previous study shows that the Raman 2D peak of BLG can be deconvoluted into four Lorentzian peaks, corresponding to the four symmetry-allowed double-resonance electron−phonon scattering processes generated by splitting parabolic bands of the AB stacking order in BLG.[23] Upon determination, the selected SLG and BLG flakes were immersed in an organic H^+ electrolyte, bis(trifluoromethane)sulfonimide (HTFSI) dissolved in poly(ethylene glycol)[20] with a concentration of 0.2 mol L^{-1}, which provides sufficient dissociative H^+ ions and a wide electrochemical window. Gold (Au) drain and source electrodes were deposited on SLG and BLG samples to establish the connection with the external circuit. A platinum (Pt) foil was used as the gate electrode, controlling the relative potential of

https://doi.org/10.1021/prechem.5c00315
Precis. Chem. XXXX, XXX, XXX−XXX

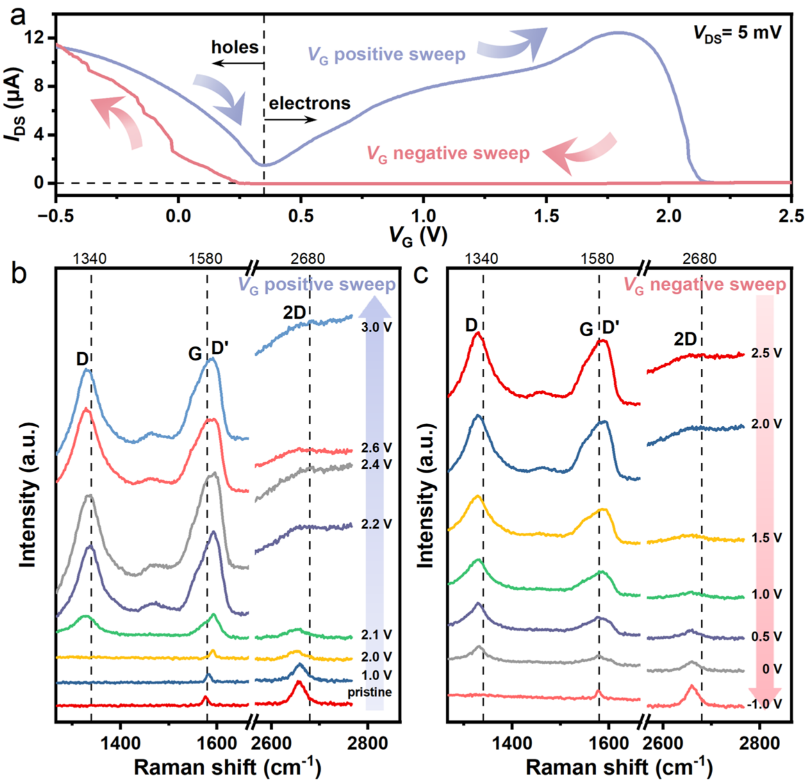

Figure 2. Conductor−insulator transition of SLG induced by hydrogenation. (a) I_{DS} dependence on gate voltage V_G (−0.5 to 2.5 V). *In situ* Raman spectra of SLG at different V_G with a sweeping rate of 5 mV s^{-1} in (b) positive and (c) negative sweeps.

graphene and the electrochemical process. Previous studies have shown that when a positive gate voltage (V_G) is applied, the Fermi level of graphene is uplifted above the Dirac point, resulting in an increased electron density of states.[20,24,25] At the same time, H$^+$ was adsorbed on graphene, forming an electric double layer. Based on such a FET device, the possible hydrogenation and dehydrogenation of graphene could be monitored by Raman spectroscopy as well as electrical conductivity testing.

Reversible Hydrogenation of SLG

To evaluate the feasibility of electric-field-controlled surface modification on graphene, the evolution of structure and electrical conductivity has been first investigated on SLG in electrochemical scanning. Figure 2a shows the drain−source current (I_{DS}) of a SLG FET device as a function of V_G. As V_G is swept positively from −0.5 to 1.7 V, the I_{DS}−V_G curve presents a typical V-shape profile related to the linear dispersion near the Dirac point in the band structure of SLG.[26] The voltage of charge neutrality point (V_{CNP}) is located at ∼0.35 V, which is attributed to p-type doping caused by charged impurity on the substrate and adsorbed electrolyte ions on SLG.[27] Further increasing V_G to 1.8 V leads to a plateau value of I_{DS} at about 12.4 μA, showing a saturated current density under gate potentials, which may originate from the enhanced scattering between carriers.[28] As V_G is increased above a critical potential of ∼2.0 V, I_{DS} rapidly drops to a very low level (nearly zero), and the resistance of SLG becomes extremely high, indicating a conductor−insulator transition. The large band gap opening at such a potential can be explained by the breaking of π conjugation caused by hydrogenation. When V_G is increased to 2.5 V and then swept back, I_{DS} remains at nearly zero value until 0.25 V. Further decreasing V_G from 0.25 to −0.5 V results in a gradual increase of I_{DS}, which finally recovers to the initial value at −0.5 V, indicating the dehydrogenation of SLG. Such a reversible conductor−insulator transition demonstrates the feasibility of controlling the hydrogenation of graphene by electric field.

The structural evolution of SLG caused by hydrogenation was investigated by *in situ* Raman spectroscopy. Figure 2b shows the Raman spectra of SLG at different V_G values during the positive sweep in cyclic voltammetry (CV) testing. Before applying the bias, only the G peak at ∼1577 cm^{-1} and 2D peak at ∼2660 cm^{-1} can be observed, associated with the in-plane E_{2g} vibrational mode and two-phonon intervalley triple resonance scattering, respectively.[23] As V_G is gradually increased to 2.0 V, the G peak blue shifts, and the 2D peak red shifts and becomes weaker/wider, caused by the heavier electron doping in graphene.[29] Further increasing V_G to 2.1 V leads to the widening and strengthening of the G peak. At the same time, the appearance of prominent yet wide D peak at 1330 cm^{-1} and D′ peak at 1600 cm^{-1}, resulting from the defect-activated intervalley and intravalley double-resonance Raman process, respectively,[23] indicates the breaking of in-plane translational symmetry in SLG caused by the formation of sp^3 C−H bonds.[10] When V_G is increased to values above 2.2 V, D, G, and 2D peaks further widen and I_{2D}/I_G decreases, revealing the higher defect density of SLG in further hydrogenation.[30] Meanwhile, the intensity of all peaks is significantly strengthened with the emergence of strong fluorescence background, which may be related to the surface-enhanced Raman scattering (SERS) effect,[31,32] probably caused by the formation of a large number of isolated sp^2 nanodomains embedded in hydrogenated sp^3 regions.[33] In addition, a new peak centered at 1460 cm^{-1} appears when V_G ≥ 2.2 V, which has not been clarified before and will be further

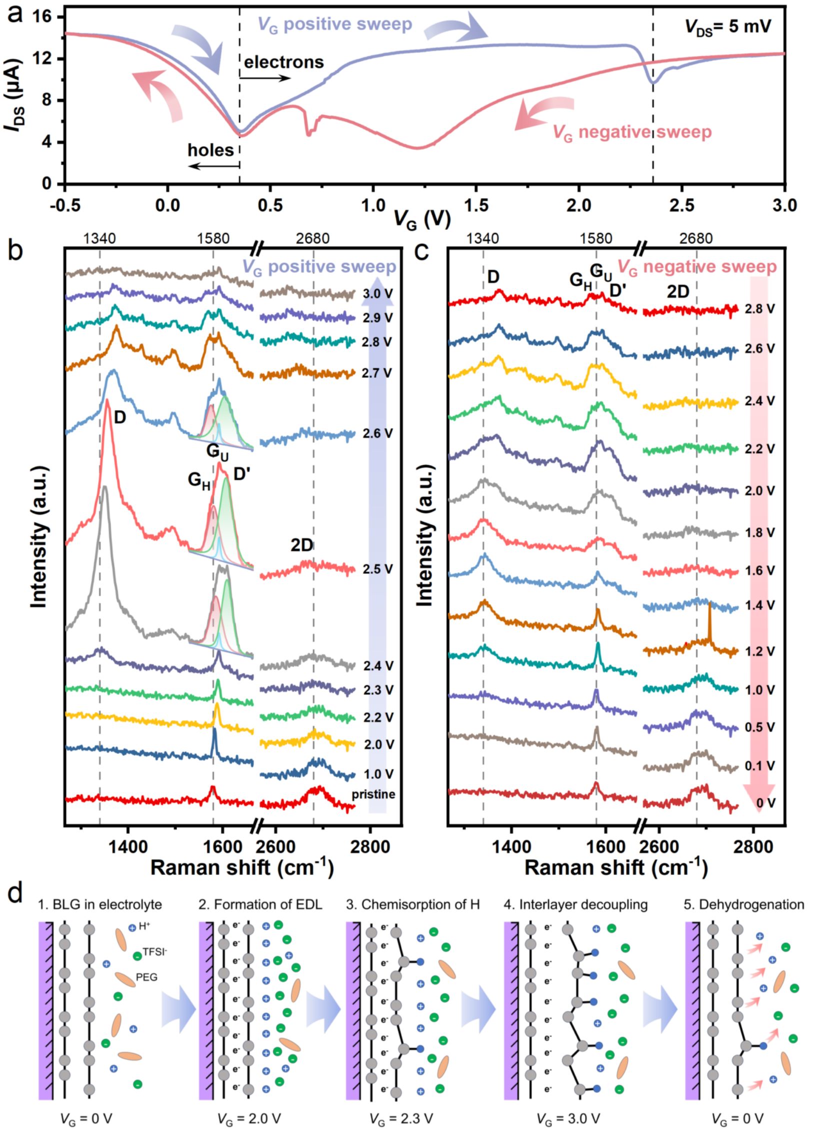

Figure 3. Conductivity and structural evolution of BLG under electrochemical gate. (a) I_{DS} of BLG FET as a function of gate voltage V_G (−0.5 to 3.0 V). *In situ* Raman spectra of BLG in (b) positive and (c) negative sweeps with a sweeping rate of 5 mV s^{-1}. The fitted contributions of G_H, G_U, and D′ for 2.4−2.6 V in panel (b) are denoted as red, blue, and green peaks, respectively. (d) Schematic diagram of the structural evolution of BLG during hydrogenation.

discussed below. The Raman characteristics remain unchanged when V_G is further increased to 3.0 V, demonstrating that the structure of graphene is no longer changed, and the hydrogenation reaches saturation. As V_G is swept back from 3.0 V, as shown in Figure 2c, Raman peaks show no changes until 2.0 V. Further decreasing V_G leads to the gradual weakening of D, G, and D′ peaks with the strengthening of 2D peak, indicating the gradual recovery of pristine sp^2 lattice and desorption of H atoms. When V_G is decreased to −1.0 V, D and D′ peaks completely disappear with only G and 2D peaks left, suggesting the complete dehydrogenation of graphene yet without damaging the graphene lattice.

The results above clearly show a H$^+$ gate-induced reversible hydrogenation of SLG, which leads to a reversible conductor−insulator transition. The hysteresis in I_{DS} curves and Raman spectra during the positive and negative sweeps suggest different kinetics on SLG during adsorption/hydrogenation and desorption/dehydrogenation. The Raman spectra complete the evolution within a narrow range of V_G above the hydrogenation potential and maintain nearly unchanged above 2.2 V, indicating that the hydrogenation of SLG reaches saturation in a narrow range of V_G. The appearance of the SERS effect and fluorescence background suggests that there are numerous sp^2 domains embedded in consecutive sp^3 regions after saturated hydrogenation. Such a hydrogenation/dehydrogenation process is different when the interlayer coupling is considered as for the situation of BLG.

Gate-Dependent Hydrogenation of BLG

Figure 3a shows the I_{DS}−V_G curve of BLG under electrochemical gate potentials, which features a V shape at a low |V_G−V_{CNP}| range and exhibits a conductivity saturation at V_G ≈ 1.5 V, indicating that the sole physical adsorption of H$^+$ and charge doping occur on BLG at this voltage. As V_G is increased to above ∼2.25 V, I_{DS} starts to decrease, suggesting the occurrence of hydrogenation. Such a critical hydrogenation potential of BLG is slightly higher than ∼2.0 V of SLG, which is related to different chemical activities and carrier transport

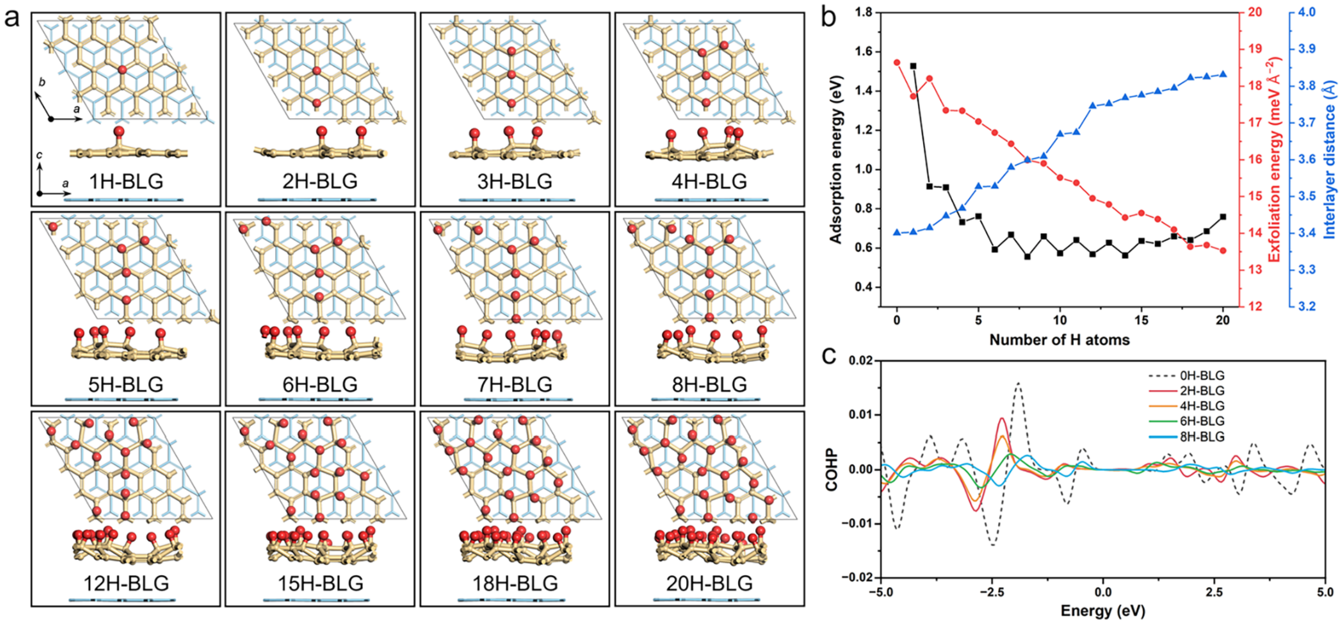

Figure 4. DFT calculations of interlayer coupling of BLG upon hydrogenation. (a) Optimized structures of BLG when adsorbing different numbers of H atoms. The bottom graphene layer in BLG is shown in cyan, the top graphene layer in BLG is shown in yellow, and the adsorbed H atoms are shown in red. (b) Average adsorption energy of each hydrogen atom adsorbed on the upper surface of BLG, interlayer distance, and interlayer exfoliation energy for BLG with different numbers of adsorbed H atoms. (c) Calculated crystal orbital Hamilton populations between the top and bottom graphene layers of 0H-BLG, 2H-BLG, 4H-BLG, 6H-BLG, and 8H-BLG.

properties in BLG caused by interlayer interaction.[30,34] After hydrogenation, the I_{DS}−V_G curve of BLG shows a very peculiar behavior compared to SLG: further increasing V_G to above 2.35 V leads to an increase in I_{DS}, and finally I_{DS} reaches a plateau value of ∼12.5 μA at V_G = 3.0 V. Our results are in good agreement with previous works on the single-sided modification of BLG with fluorine or oxygen.[18,30] Considering the different I_{DS}−V_G responses for SLG and BLG, we propose that the hydrogenation preferentially occurs at one of the two layers in BLG, where the C−H bonding significantly disrupts the π conjugation and leads to an interlayer decoupling. The absence of a conductor−insulator transition even for a higher V_G of 4.0 V (Figure S1) suggests that the other layer in BLG remains almost intact, leading to a conductance like electron-doped SLG in Figure 2a. In addition, Figure 3a shows that when V_G is swept back from 3.0 V, I_{DS} gradually decreases until 1.2 V and then increases, which may be related to the desorption of H and recovery of interlayer coupling. As V_G is decreased to a voltage below 0.6 V, the I_{DS}−V_G curve eventually coincides with the original V-shaped profile in the positive sweep, corresponding to the nearly complete dehydrogenation of BLG.

To verify the preferential hydrogenation in one layer of BLG, *in situ* Raman spectra of BLG at 0 V < V_G < 3.0 V were obtained in a CV cycle with a scanning rate of 5 mV s^{-1}, and the corresponding CV curve is shown in Figure S2. Figure 3b shows that when V_G is lower than 2.2 V in the positive sweep, only G and 2D peaks can be observed, similar to the situation of SLG below 2.0 V. As V_G reaches the hydrogenation potential of ∼2.3 V, the appearance of D peak at ∼1341 cm^{-1} and D′ peak at ∼1614 cm^{-1} in Raman spectra indicates the generation of defects caused by chemisorption of H$^+$, corresponding to the drop of I_{DS} at V_G above 2.25 V. When V_G increases to 2.4 V, the intensity of D and D′ peaks significantly increases compared to that of the 2D peak, due to the large increase in the density of defects during hydrogenation. At the same time, the overall Raman intensity is significantly enhanced due to the SERS effect of sp^2 domains.[33,35] The significant blue shift of D peak may be attributed to the increased compressive stress caused by structural distortion during hydrogenation.[36] Meanwhile, the G peak becomes wider/stronger and merges with the D′ peak to form a wide peak. The abovementioned Raman features observed at 2.4 V agree well with the decline of I_{DS} at 2.25 V < V_G < 2.35 V, when the π conjugation is partially broken.[37,38] Very interestingly, new peaks at 1400−1430 and 1460−1530 cm^{-1} have been observed, which shall be related to specific C−C vibrations in the localized hydrogenation structure and will be discussed in detail later. As V_G is further increased from 2.4 to 2.9 V, the D peak shows a constant blue shift, indicating increased structural stress. Meanwhile, the Raman signal-to-noise ratio is significantly reduced, which might be due to the weakening of the SERS effect as the fraction of isolated sp^2 domains is reduced during further hydrogenation. On the other hand, as V_G increases, the broad band at 1550−1640 cm^{-1} keeps red-shifting with its shape changing. As shown in Figure 3b (with more details in Figure S3), this broad band can be deconvoluted into three peaks (G_H, G_U, D′) by Gauss−Lorentz fitting. G_H mode originates from the vibration of sp^2-hybridized rings adjacent to hydrogenated sp^3 domains and exhibits a red shift from 1586 to 1572 cm^{-1}, due to the reduced force constant of carbon bonds by hydrogenation.[39] G_U mode centered at 1592 cm^{-1} remains nearly unchanged for V_G between 2.4 and 2.9 V, highly coinciding with the G peak of intrinsic graphene contributed by large sp^2 regions. The retention of such a sharp G_U peak has been reported in the study of single-sided oxidation or fluorination of BLG.[18,30] The intensity of D′ peak centered at ∼1605 cm^{-1}, contributed from regions with abundant sp^3 C−C bonds, gradually decreases as V_G increases. At V_G = 3 V, only a G_U peak at 1592 cm^{-1} and a weak, red-shifted 2D peak can be observed, like the Raman spectrum (yellow curve at ~2.0 V in Figure 2b) of electron-doped SLG yet without hydrogenation. The evolution of Raman spectra with V_G indicates enhanced hydrogen adsorption at higher potentials, leading to distinct hydrogenation structures depending on V_G. Constant potential measurement was further conducted with each spectrum acquired after V_G was maintained at a certain voltage for 5 min, to eliminate the possible kinetic effects in CV scans. The Raman spectra (Figure S4) obtained under constant potentials exhibit features highly consistent with those presented in Figure 3b, demonstrating that the rapid hydrogenation strongly depends on the gate voltage. When the external electric field is removed, however, BLG gradually returns to the planar sp^2 structure in minutes, as shown in more Raman spectra in Figure S5.

When V_G is swept back from 3 V, as shown in Figure 3c, the D peak shows a red shift, and the intensities of both D and D′ peaks first increase and then decrease, and almost completely vanish at 0.5 V, indicating the gradual detachment of H from BLG. During dehydrogenation, G_U remains unchanged, while G_H blue shifts, weakens, and finally merges with G_U at ~1.4 V, corresponding to the reduction of stress and recovery of structural deformation. The new peaks at 1400−1430 and 1460−1530 cm^{-1} gradually weaken and eventually disappear at ~1.6 V. When V_G is decreased to 0 V, the complete vanishment of D and D′ peaks and appearance of the 2D peak indicate that BLG recovers the pristine structure with AB stacking. Figure 3d schematically shows the proposed structural evolution of BLG during hydrogenation, where the preferential adsorption of H^+ and hydrogenation on the top layer, structural deformation, and interlayer decoupling between layers sequentially occur, as motivated by the electrochemical gate potential applied. For BLG, a previous study showed that the applied electric field is strongly localized on the top layer,[20] and thus we prefer to consider that hydrogenation mainly occurs on the top layer, although Raman spectroscopy cannot be used to distinguish which layer is hydrogenated in BLG. The energy barrier (~0.2 eV) for the formation of C−H bonds[20] can be significantly reduced by heavy electron doping and strong electric fields.

Hydrogenation-Regulated Interlayer Coupling by Simulations

To further reveal the effect of surface functionalization of graphene on interlayer coupling, *ab initio* calculations were performed with DFT. The hydrogenated SLG and BLG structures were obtained by the greedy algorithm, within a 4 × 4 × 1 supercell, as illustrated in detail in Methods section. H atoms were adsorbed onto the upper surface of graphene one by one, and at each step, the most energy-favored structure was selected and named *n*H-SLG (Figure S6) or *n*H-BLG (Figure 4a), where *n* is the number of attached H atoms.

As shown in Figure 4a, the second H tends to adsorb on the para-position carbon relative to the first H adsorption. The third H is attached to the ortho-site of the first H, forming a straight line with the first two adsorbed H atoms, and the fourth H is attached to the ortho-site of the third H. To our surprise, the fifth H atom is attached to the site far from the existing four H atoms, showing that hydrogenation nucleates via a specific "C_4H_4" configuration. With more H adsorption to the coverage of 25% (8H-BLG), the formation of another "C_4H_4" nucleus adjacent to the first one is observed. Higher coverage of adsorbed H was tested until 20 H atoms, resulting in significant distortion of the carbon skeleton and interlayer separation. In addition, the hydrogenation of SLG has also been tested, showing a similar "C_4H_4" structure in the nucleation stage, although the H attachment sequence is slightly different (Figure S6). The stability of all hydrogenation structures has been verified by *ab initio* molecular dynamics (AIMD) simulations (Figures S7−S9 and Videos S1−S32). Therefore, we propose that the formation of "C_4H_4" nuclei would be a critical step during the hydrogenation of graphene.

In the structures shown in Figure 4a, the top graphene layer is found to gradually deform and detach from the bottom layer under hydrogenation. The interlayer distance is increased from 3.40 to 3.83 Å with the adsorption of more H atoms, as shown in Figure 4b, leading to a weakened interlayer interaction. On the other hand, the adsorption energy (E_{ads}) of H on BLG or SLG, which is defined by eq 1 in Methods section, is shown in Figures 4b and S10. E_{ads} values for all steps are positive, indicating that the hydrogenation of SLG and BLG requires additional energy and is thermodynamically unfavored. Figure 4b also shows that the energy needed for exfoliation of BLG is reduced from 18.6 to 13.5 meV $Å^{-2}$ as the hydrogenation increases, indicating that the top layer hydrogenation weakens the interlayer interaction of BLG. To further elucidate the electronic origin of the hydrogenation-dependent interlayer coupling, crystal orbital Hamilton population (COHP) analyses between the top and bottom graphene layers from 0H-BLG to 8H-BLG were performed. As shown in Figure 4c, the COHP intensity of hydrogenated BLG is significantly reduced compared to that of pristine BLG. For example, the integral of COHP (ICOHP) to the Fermi level decreases from −0.301 eV for 0H-BLG to −0.106 eV for 8H-BLG, when considering the interaction between all vertically aligned carbon atoms in the top and bottom layers. The lower absolute value of ICOHP indicates that the hydrogenation promotes the interlayer decoupling of BLG.

The band structures have been calculated to explain the evolution of the electronic properties of SLG and BLG under hydrogenation. For SLG (Figure S11), the chemisorption of H leads to a significant band gap opening, and the gap width increases as the hydrogenation degree increases, as shown in Figure S12. For BLG (Figures S13 and S14), the double parabolic energy dispersion near the Fermi level splits into two groups of bands upon hydrogenation. The first group of bands has a Dirac cone shape at the Fermi level, which is preserved throughout the whole hydrogenation process, originating from the intact bottom layer. The second group of bands exhibits an energy gap that becomes larger as the hydrogenation degree increases, originating from the hydrogenated top layer. The absence of an overall band gap of BLG during hydrogenation is consistent with the experimental observation that BLG maintains a high conductivity upon hydrogenation, like intact SLG.

Simulated Raman Spectra of the Localized "C_4H_4" Hydrogenation Structure

The *in situ* Raman spectroscopy has shown new Raman modes in the region between D and G peaks for hydrogenated SLG (1420−1500 cm^{-1}) and BLG (1400−1530 cm^{-1}), probably related to the formation of some widespread localized hydrogenation structures.[40−43] To verify this speculation, the Raman spectra of hydrogenated SLG have been calculated (Figure S15), showing an extra peak at 1473 cm^{-1} (6H-SLG)

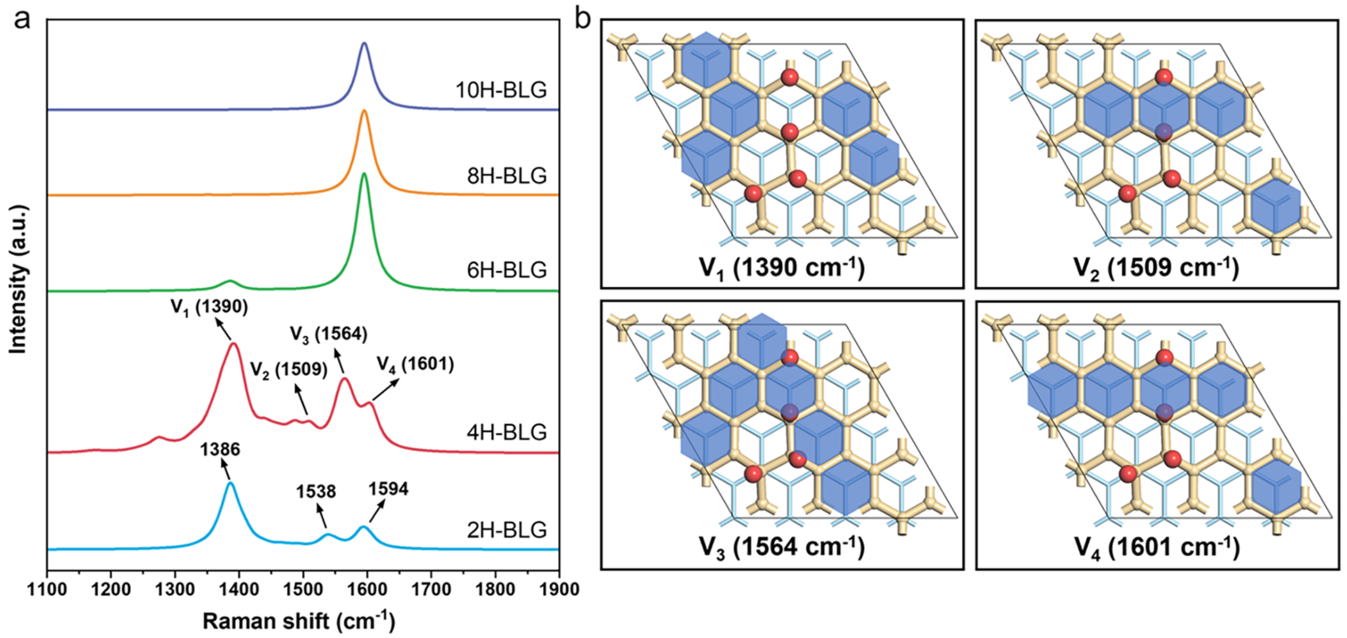

Figure 5. Characteristic Raman modes from the hydrogenation structure. (a) Simulated Raman spectra of BLG after adsorbing different numbers of H atoms on the top layer. (b) Representative vibrational modes between 1200 and 1700 cm^{-1} in the 4H-BLG model, corresponding to the peaks marked by arrows in 4H-BLG in panel (a). The bottom graphene layer in BLG is shown in cyan, the top graphene layer in BLG is shown in yellow, the adsorbed H atoms are shown in red, and the carbon rings involved in the corresponding vibrational modes are marked by blue.

originating from the C−C vibrations adjacent to the sp^3 C−H bonds, in addition to the two strong peaks at ∼1341 and 1606 cm^{-1}. For BLG (Figure 5a), upon attaching two H atoms, three obvious vibration peaks at ∼1386, ∼1538, and ∼1594 cm^{-1} are determined. For 4H-BLG containing "C_4H_4" nuclei, four main peaks at ∼1390, 1509, 1564, and 1601 cm^{-1} are obtained with their corresponding vibrations shown in Figure 5b. These modes mainly originate from the vibrations of carbon rings with adsorbed H atoms, or the rings adjacent to them, as shown by a more vivid illustration in Videos S33−S41. When attaching 6 or more H atoms, the simulated Raman spectra of BLG become the same as that of the unfunctionalized SLG. By separately simulating the Raman spectra of the top and bottom layers in 8H-BLG (Figure S16), we find that these vibration peaks at 1200−1600 cm^{-1} exclusively belong to the top hydrogenated layer, while the bottom intact layer exhibits the same Raman feature as SLG, which is strong enough to cover the signal from the top layer. Such simulation results fully support our experimental observation for BLG at V_G of 3.0 V. Furthermore, these four peaks maintain their positions even for the calculations based on a larger 6 × 6 × 1 supercell (Figure S17) and the different distribution of H adsorption sites does not disturb the appearance of Raman modes at 1400−1530 cm^{-1} (Figure S18), proving the robustness of new Raman modes upon hydrogenation in our studies.

CONCLUSIONS

In conclusion, we demonstrate that electrochemical hydrogenation can achieve reversible chemical functionalization and interlayer coupling/decoupling of BLG, controlled by the gate voltage. By combining conductivity measurements, Raman spectroscopy studies, and DFT simulations, our results show that the bonding of H atoms on graphene leads to the formation of an insulative, continuous sp^3 C−H network with isolated sp^2 nanodomains embedded. An intermediate nucleation structure of "C_4H_4" is proposed. The distorted lattice of the hydrogenated graphene layer leads to a significant decoupling with the other layer, and the whole structure exhibits continuous electron conduction with new Raman peaks appearing at 1400−1530 cm^{-1}, related to the vibration of distorted carbon rings adjacent to sp^3 C−H bonds. Our work unveils the correlation between the interlayer interaction and surface structure, providing deeper understanding for the study of the surface and interface in 2D graphene stackings.

METHODS

Fabrication of the Graphene Electrochemical Gating Device

Graphene flakes were prepared on Si substrates (300 nm SiO_2) by modified mechanical exfoliation of natural graphite (20−25 mm, Germany NGS). For exfoliation, the Si substrates were cleaned with oxygen plasma, and adhesive tapes with graphite flakes were sticked onto these substrates followed by heating on a hot plate at ∼100 °C for 2 min. The layer number and size of the as-obtained graphene flakes were identified using optical microscopy and Raman spectroscopy. The graphene FETs were fabricated by electron-beam lithography and depositing Cr/Au (10/100 nm) as drain and source electrodes on graphene flakes by using electron-beam evaporation. Then, 300 nm poly(methyl methacrylate) (PMMA) was spin-coated onto the entire silicon wafer to avoid contact between metal electrodes and electrolyte, followed by opening windows above the FET channel using electron-beam lithography. A Pt wire was rolled into a thin sheet (20 mm × 1 mm × 30 μm) to serve as a gate electrode. All electrodes were sealed into an electrolyte cell constructed between a Si substrate and a thin cover glass using a hot melt adhesive film (polyurethane, 60 μm). Two little openings were reserved for filling the electrolyte by capillary effect. The thickness of the electrolyte was determined by the gap between the substrate and cover glass. The injection of H^+ electrolyte was carried out in an Ar-filled glovebox and the filling openings were fully sealed with epoxy resin before the cell was taken out of the glovebox for electrical and spectral tests in air. The H^+ electrolyte with a concentration of 0.2 mol L^{-1} was prepared by dissolving bis-

(trifluoromethane)sulfonamide (HTFSI) in liquid poly(ethylene glycol) (PEG) with a number-averaged molecular weight (M_n) of 600. A PEG solvent was pretreated with a molecular sieve and vacuum drying to remove water. The preparation and injection of electrolyte were all carried out in an argon-filled glovebox.

Electrical Measurement

Electrical measurement was carried out using a Keithley 4200 meter. A sweeping bias V_G was applied between the Pt gate electrode and graphene electrode, and the voltage V_{DS} between drain and source electrodes was fixed at 5 mV to measure I_{DS} synchronously. All the electric experiments were repeated several times to ensure the reliability of data.

Raman Spectroscopy

In situ Raman spectroscopy was conducted in cyclic voltammetry testing from 0 to 3.0 V with a sweeping rate of 5 mV s^{-1} using a PARSTAT MC electrochemical workstation (Princeton Company, USA). Raman spectra were acquired using a Renishaw instrument with 532 nm laser, 1800 l/mm grating, ×50 objective lens with ∼1-μm-diameter spot size, and a motorized XYZ stage. To get better signal of graphene in the electrolyte, a power of 25 mW was used with an acquisition of 3 s and the background signals from the electrolyte, cover glass, and silicon substrates were subtracted when analyzing the data. The raw Raman spectra (without background subtraction) and the Raman spectrum of pure electrolyte are provided in Figure S19.

Theoretical Calculations

DFT[44] calculations were carried out using projector-augmented wave pseudopotentials[45] as adopted in the Vienna ab initio simulation package (VASP).[46−48] Exchange correlation interactions were described by the Perdew−Burke−Ernzerhof (PBE)[49] generalized gradient approximation (GGA).[50] Becke−Jonson damping DFT-D3 correction was used.[51] Raman spectra were calculated by a Raman off-resonance activity calculator in combination with VASP, which was developed by Alexandr Fonari (Georgia Tech) and Shannon Stauffer (UT Austin), available at https://github.com/afonari/raman-sc. The Crystal Orbital Hamilton Population (COHP) calculations were performed by LOBSTER software[52] based on the electronic structure calculations by VASP.

We applied a slab approach with vacuum layers of 15 Å to decouple periodic images from each other along the *z* direction. For hexagonal (4 × 4) unit cell H-SLG with 32 carbon atoms and H-BLG with 64 carbon atoms, the plane wave kinetic energy cutoff was set to be 500 eV. To ensure stable geometry, the force convergence was set to be 0.01 eV $Å^{-1}$ and the structural optimization convergence criterion was set to be 10^{-5} eV in energy. Brillouin zone was represented by a γ-centered *k*-point mesh of 4 × 4 × 1 for structure optimization, Raman spectrum, and COHP calculations. For hexagonal (6 × 6) unit cell H-SLG with 100 carbon atoms, Brillouin zone was represented by γ special *k*-point mesh of 1 × 1 × 1. The average adsorption energy of H atoms onto graphene is calculated by the following formula

$$E_{\mathrm{ads}} = \frac{E_{n\mathrm{H+C}} - E_{\mathrm{gra}} - n \times E_{\mathrm{H}}}{n} \quad (1)$$

We employed a greedy algorithm-based sequential structure growth approach to construct hydrogenated graphene models. Starting from a graphene structure with a given hydrogen coverage, all possible hydrogen adsorption sites are enumerated (Figure S20), and one additional hydrogen atom is introduced at each step. The total energies of the resulting configurations are evaluated using DFT optimizations, and the structure with the lowest energy is selected as the initial configuration for the next step (Tables S1 and S2). This procedure is repeated iteratively until the target hydrogen coverage is reached.

Ab initio molecular dynamics (AIMD) simulations were carried out with VASP software, under 300 K temperature and NVT ensemble. The simulation time step is 1 fs, and the number of simulation steps is 5000. Brillouin zone was sampled by a γ-centered *k*-point mesh of 2 × 2 × 1.

■ ASSOCIATED CONTENT

SI Supporting Information

The Supporting Information is available free of charge at https://pubs.acs.org/doi/10.1021/prechem.5c00315.

> Videos showing the structural evolutions of *n*H-SLG and *n*H-BLG in the AIMD simulation; videos showing the carbon ring vibration modes corresponding to the Raman peaks at 1390, 1509, 1564, and 1601 cm^{-1} (ZIP)
>
> Additional I_{DS}−V_G and CV curves of BLG; magnified Raman spectra of BLG at high V_G; Raman spectra of BLG under constant potential measurement; time-dependent Raman spectra of hydrogenated BLG after removing V_G; simulated hydrogenation structures of *n*H-SLG; AIMD simulations of the change of potential energy of *n*H-SLG and *n*H-BLG with simulation step; H adsorption energy calculation on SLG during hydrogenation; calculated band structures of *n*H-SLG and *n*H-BLG; simulated Raman spectra of *n*H-SLG; simulated Raman spectra of the top/bottom layer in interlayer-separated 8H-BLG; simulated Raman spectra of 4H-BLG, 2H-BLG, and 6H-BLG with different configurations using a 6 × 6 × 1 unit cell; raw Raman spectra without background subtraction and Raman spectrum of pure electrolyte; H adsorption positions and calculated structural energies during the hydrogenation of SLG and BLG (PDF)

■ AUTHOR INFORMATION

Corresponding Authors

Kun Ni − *Department of Materials Science and Engineering, School of Chemistry and Materials Science, University of Science and Technology of China, Hefei 230026, China; State Key Laboratory of Precision and Intelligent Chemistry, University of Science and Technology of China, Hefei 230026, China*; Email: nikun@ustc.edu.cn

Yanwu Zhu − *Department of Materials Science and Engineering, School of Chemistry and Materials Science, University of Science and Technology of China, Hefei 230026, China; Hefei National Research Center for Physical Sciences at the Microscale and State Key Laboratory of Precision and Intelligent Chemistry, University of Science and Technology of China, Hefei 230026, China*; orcid.org/0000-0002-7505-1502; Email: zhuyanwu@ustc.edu.cn

Authors

Yanbo Zhang − *Department of Materials Science and Engineering, School of Chemistry and Materials Science, University of Science and Technology of China, Hefei 230026, China; State Key Laboratory of Precision and Intelligent Chemistry, University of Science and Technology of China, Hefei 230026, China*

Yizhe Wang − *Hefei National Research Center for Physical Sciences at the Microscale, University of Science and Technology of China, Hefei 230026, China*

Wenchang Zhang − *Department of Materials Science and Engineering, School of Chemistry and Materials Science, University of Science and Technology of China, Hefei 230026, China; State Key Laboratory of Precision and Intelligent Chemistry, University of Science and Technology of China, Hefei 230026, China*

Na Shu − *Department of Materials Science and Engineering, School of Chemistry and Materials Science, University of Science and Technology of China, Hefei 230026, China; State Key Laboratory of Precision and Intelligent Chemistry, University of Science and Technology of China, Hefei 230026, China*

Xiaolan Wang − *Department of Materials Science and Engineering, School of Chemistry and Materials Science, University of Science and Technology of China, Hefei 230026, China; State Key Laboratory of Precision and Intelligent Chemistry, University of Science and Technology of China, Hefei 230026, China*

Yan Yu − *Department of Materials Science and Engineering, School of Chemistry and Materials Science, University of Science and Technology of China, Hefei 230026, China;* orcid.org/0000-0002-3685-7773

Complete contact information is available at: https://pubs.acs.org/10.1021/prechem.5c00315

Author Contributions

∥Y.B.Z. and Y.Z.W. contributed equally to this work. Y.W.Z. and K.N. proposed the idea and supervised the research. Y.B.Z., N.S., and X.L.W. fabricated the devices and carried out the electrical transport and Raman spectroscopy test. Y.B.Z. and W.C.Z. analyzed the data. Y.Z.W. performed theoretical calculations. Y.B.Z., Y.Z.W., Y.Y., K.N., and Y.W.Z. prepared the manuscript.

Notes

The authors declare no competing financial interest.

■ ACKNOWLEDGMENTS

This work was supported by the National Natural Science Foundation of China (Nos. 52273234 and 52325202); The Fundamental Research Funds for the Central Universities (WK2060000098 and WK9990000170); and the open research fund of State Key Laboratory of Precision and Intelligent Chemistry (KY2490000300). The USTC Center for Micro and Nanoscale Research and Fabrication, the Supercomputing Center of USTC, and the Hefei Advanced Computing Center are appreciated.

■ REFERENCES

(1) Kroemer, H. Nobel Lecture: Quasielectric Fields and Band Offsets: Teaching Electrons New Tricks. *Rev. Mod. Phys.* **2001**, *73* (3), 783−793.

(2) Tsukazaki, A.; Akasaka, S.; Nakahara, K.; Ohno, Y.; Ohno, H.; Maryenko, D.; Ohtomo, A.; Kawasaki, M. Observation of the Fractional Quantum Hall Effect in an Oxide. *Nat. Mater.* **2010**, *9* (11), 889−893.

(3) Reyren, N.; Thiel, S.; Caviglia, A. D.; Kourkoutis, L. F.; Hammerl, G.; Richter, C.; Schneider, C. W.; Kopp, T.; Rüetschi, A.-S.; Jaccard, D.; Gabay, M.; Muller, D. A.; Triscone, J.-M.; Mannhart, J. Superconducting Interfaces Between Insulating Oxides. *Science* **2007**, *317* (5842), 1196−1199.

(4) Bhattacharya, A.; May, S. J.; te Velthuis, S. G. E.; Warusawithana, M.; Zhai, X.; Jiang, B.; Zuo, J.-M.; Fitzsimmons, M. R.; Bader, S. D.; Eckstein, J. N. Metal-Insulator Transition and Its Relation to Magnetic Structure in (LaMnO3)2n/(SrMnO3)n Superlattices. *Phys. Rev. Lett.* **2008**, *100* (25), No. 257203.

(5) Georgakilas, V.; Otyepka, M.; Bourlinos, A. B.; Chandra, V.; Kim, N.; Kemp, K. C.; Hobza, P.; Zboril, R.; Kim, K. S. Functionalization of Graphene: Covalent and Non-Covalent Approaches, Derivatives and Applications. *Chem. Rev.* **2012**, *112* (11), 6156−6214.

(6) Johns, J. E.; Hersam, M. C. Atomic Covalent Functionalization of Graphene. *Acc. Chem. Res.* **2013**, *46* (1), 77−86.

(7) Dou, Z.; Chen, Z.; Li, N.; Yang, S.; Yu, Z.; Sun, Y.; Li, Y.; Liu, B.; Luo, Q.; Ma, T.; Liao, L.; Liu, Z.; Gao, P. Atomic Mechanism of Strong Interactions at the Graphene/Sapphire Interface. *Nat. Commun.* **2019**, *10* (1), No. 5013.

(8) Zhao, J.; Ji, P.; Li, Y.; Li, R.; Zhang, K.; Tian, H.; Yu, K.; Bian, B.; Hao, L.; Xiao, X.; Griffin, W.; Dudeck, N.; Moro, R.; Ma, L.; de Heer, W. A. Ultrahigh-Mobility Semiconducting Epitaxial Graphene on Silicon Carbide. *Nature* **2024**, *625* (7993), 60−65.

(9) Błoński, P.; Tuček, J.; Sofer, Z.; Mazánek, V.; Petr, M.; Pumera, M.; Otyepka, M.; Zbořil, R. Doping with Graphitic Nitrogen Triggers Ferromagnetism in Graphene. *J. Am. Chem. Soc.* **2017**, *139* (8), 3171−3180.

(10) Elias, D. C.; Nair, R. R.; Mohiuddin, T. M. G.; Morozov, S. V.; Blake, P.; Halsall, M. P.; Ferrari, A. C.; Boukhvalov, D. W.; Katsnelson, M. I.; Geim, A. K.; Novoselov, K. S. Control of Graphene's Properties by Reversible Hydrogenation: Evidence for Graphane. *Science* **2009**, *323* (5914), 610−613.

(11) Yu, M.; Chen, C.; Liu, Q.; Mattioli, C.; Sang, H.; Shi, G.; Huang, W.; Shen, K.; Li, Z.; Ding, P.; Guan, P.; Wang, S.; Sun, Y.; Hu, J.; Gourdon, A.; Kantorovich, L.; Besenbacher, F.; Chen, M.; Song, F.; Rosei, F. Long-Range Ordered and Atomic-Scale Control of Graphene Hybridization by Photocycloaddition. *Nat. Chem.* **2020**, *12* (11), 1035−1041.

(12) Wu, F.; Das Sarma, S. Collective Excitations of Quantum Anomalous Hall Ferromagnets in Twisted Bilayer Graphene. *Phys. Rev. Lett.* **2020**, *124* (4), No. 046403.

(13) Cao, Y.; Fatemi, V.; Demir, A.; Fang, S.; Tomarken, S. L.; Luo, J. Y.; Sanchez-Yamagishi, J. D.; Watanabe, K.; Taniguchi, T.; Kaxiras, E.; Ashoori, R. C.; Jarillo-Herrero, P. Correlated Insulator Behaviour at Half-Filling in Magic-Angle Graphene Superlattices. *Nature* **2018**, *556* (7699), 80−84.

(14) Cao, Y.; Fatemi, V.; Fang, S.; Watanabe, K.; Taniguchi, T.; Kaxiras, E.; Jarillo-Herrero, P. Unconventional Superconductivity in Magic-Angle Graphene Superlattices. *Nature* **2018**, *556* (7699), 43−50.

(15) Ni, K.; Du, J.; Yang, J.; Xu, S.; Cong, X.; Shu, N.; Zhang, K.; Wang, A.; Wang, F.; Ge, L.; Zhao, J.; Qu, Y.; Novoselov, K. S.; Tan, P.; Su, F.; Zhu, Y. Stronger Interlayer Interactions Contribute to Faster Hot Carrier Cooling of Bilayer Graphene under Pressure. *Phys. Rev. Lett.* **2021**, *126* (2), No. 027402.

(16) Zhao, W.; Tan, P.; Liu, J.; Ferrari, A. C. Intercalation of Few-Layer Graphite Flakes with FeCl3: Raman Determination of Fermi Level, Layer by Layer Decoupling, and Stability. *J. Am. Chem. Soc.* **2011**, *133* (15), 5941−5946.

(17) Lin, Y.-C.; Motoyama, A.; Solís-Fernández, P.; Matsumoto, R.; Ago, H.; Suenaga, K. Coupling and Decoupling of Bilayer Graphene Monitored by Electron Energy Loss Spectroscopy. *Nano Lett.* **2021**, *21* (24), 10386−10391.

(18) Son, J.; Ryu, H.; Kwon, J.; Huang, S.; Yu, J.; Xu, J.; Watanabe, K.; Taniguchi, T.; Ji, E.; Lee, S.; Shin, Y.; Kim, J. H.; Kim, K.; van der Zande, A. M.; Lee, G.-H. Tailoring Single- and Double-Sided Fluorination of Bilayer Graphene via Substrate Interactions. *Nano Lett.* **2021**, *21* (2), 891−898.

(19) Xuan, N.; Xie, A.; Liu, B.; Sun, Z. Tuning Electrical Coupling in Bilayer Graphene. *Carbon* **2023**, *201*, 529−534.

(20) Li, S.; Li, J.; Wang, Y.; Yu, C.; Li, Y.; Duan, W.; Wang, Y.; Zhang, J. Large Transport Gap Modulation in Graphene via Electric-Field-Controlled Reversible Hydrogenation. *Nat. Electron.* **2021**, *4* (4), 254−260.

(21) He, Q.; Zeng, L.; Han, L.; Sartin, M. M.; Peng, J.; Li, J.-F.; Oleinick, A.; Svir, I.; Amatore, C.; Tian, Z.-Q.; Zhan, D. Electrochemical Storage of Atomic Hydrogen on Single Layer Graphene. *J. Am. Chem. Soc.* **2021**, *143* (44), 18419−18425.

(22) Mag-isa, A. E.; Lee, C.-K.; Kim, S.-M.; Kim, J.-H.; Oh, C.-S. Rapid Determination of the Number of Graphene Layers by Using Relative Luminance. *Carbon* **2015**, *94*, 646−649.

(23) Malard, L. M.; Pimenta, M. A.; Dresselhaus, G.; Dresselhaus, M. S. Raman Spectroscopy in Graphene. *Phys. Rep.* **2009**, *473* (5−6), 51−87.

(24) Tong, J.; Fu, Y.; Domaretskiy, D.; Della Pia, F.; Dagar, P.; Powell, L.; Bahamon, D.; Huang, S.; Xin, B.; Costa Filho, R. N.; Vega, L. F.; Grigorieva, I. V.; Peeters, F. M.; Michaelides, A.; Lozada-Hidalgo, M. Control of Proton Transport and Hydrogenation in Double-Gated Graphene. *Nature* **2024**, *630* (8017), 619−624.

(25) Binder, J.; Urban, J. M.; Stepniewski, R.; Strupinski, W.; Wysmolek, A. In Situ Raman Spectroscopy of the Graphene/Water Interface of a Solution-Gated Field-Effect Transistor: Electron−Phonon Coupling and Spectroelectrochemistry. *Nanotechnology* **2016**, *27* (4), No. 045704.

(26) Neto, A. H. C.; Guinea, F.; Peres, N. M. R.; Novoselov, K. S.; Geim, A. K. The Electronic Properties of Graphene. *Rev. Mod. Phys.* **2009**, *81* (1), 109−162.

(27) Tan, Y.-W.; Zhang, Y.; Bolotin, K.; Zhao, Y.; Adam, S.; Hwang, E. H.; Das Sarma, S.; Stormer, H. L.; Kim, P. Measurement of Scattering Rate and Minimum Conductivity in Graphene. *Phys. Rev. Lett.* **2007**, *99* (24), No. 246803.

(28) Efetov, D. K.; Kim, P. Controlling Electron-Phonon Interactions in Graphene at Ultrahigh Carrier Densities. *Phys. Rev. Lett.* **2010**, *105* (25), No. 256805.

(29) Das, A.; Pisana, S.; Chakraborty, B.; Piscanec, S.; Saha, S. K.; Waghmare, U. V.; Novoselov, K. S.; Krishnamurthy, H. R.; Geim, A. K.; Ferrari, A. C.; Sood, A. K. Monitoring Dopants by Raman Scattering in an Electrochemically Top-Gated Graphene Transistor. *Nat. Nanotechnol.* **2008**, *3* (4), 210−215.

(30) Felten, A.; Flavel, B. S.; Britnell, L.; Eckmann, A.; Louette, P.; Pireaux, J.; Hirtz, M.; Krupke, R.; Casiraghi, C. Single- and Double-Sided Chemical Functionalization of Bilayer Graphene. *Small* **2013**, *9* (4), 631−639.

(31) Faggio, G.; Grillo, R.; Lisi, N.; Buonocore, F.; Chierchia, R.; Jung Kim, M.; Lee, G.-H.; Capasso, A.; Messina, G. Nanocrystalline Graphene for Ultrasensitive Surface-Enhanced Raman Spectroscopy. *Appl. Surf. Sci.* **2022**, *599*, No. 154035.

(32) Wang, Z.; Wu, S.; Ciacchi, L. C.; Wei, G. Graphene-Based Nanoplatforms for Surface-Enhanced Raman Scattering Sensing. *Analyst* **2018**, *143* (21), 5074−5089.

(33) Schäfer, R. A.; Englert, J. M.; Wehrfritz, P.; Bauer, W.; Hauke, F.; Seyller, T.; Hirsch, A. On the Way to Graphane—Pronounced Fluorescence of Polyhydrogenated Graphene. *Angew. Chem., Int. Ed.* **2013**, *52* (2), 754−757.

(34) Koehler, F. M.; Jacobsen, A.; Ensslin, K.; Stampfer, C.; Stark, W. J. Selective Chemical Modification of Graphene Surfaces: Distinction Between Single- and Bilayer Graphene. *Small* **2010**, *6* (10), 1125−1130.

(35) Luo, Z.; Yu, T.; Ni, Z.; Lim, S.; Hu, H.; Shang, J.; Liu, L.; Shen, Z.; Lin, J. Electronic Structures and Structural Evolution of Hydrogenated Graphene Probed by Raman Spectroscopy. *J. Phys. Chem. C* **2011**, *115* (5), 1422−1427.

(36) Ni, Z. H.; Wang, H. M.; Ma, Y.; Kasim, J.; Wu, Y. H.; Shen, Z. X. Tunable Stress and Controlled Thickness Modification in Graphene by Annealing. *ACS Nano* **2008**, *2* (5), 1033−1039.

(37) Balog, R.; Jørgensen, B.; Nilsson, L.; Andersen, M.; Rienks, E.; Bianchi, M.; Fanetti, M.; Lægsgaard, E.; Baraldi, A.; Lizzit, S.; Sljivancanin, Z.; Besenbacher, F.; Hammer, B.; Pedersen, T. G.; Hofmann, P.; Hornekær, L. Bandgap Opening in Graphene Induced by Patterned Hydrogen Adsorption. *Nat. Mater.* **2010**, *9* (4), 315−319.

(38) Betti, M. G.; Placidi, E.; Izzo, C.; Blundo, E.; Polimeni, A.; Sbroscia, M.; Avila, J.; Dudin, P.; Hu, K.; Ito, Y.; Prezzi, D.; Bonacci, M.; Molinari, E.; Mariani, C. Gap Opening in Double-Sided Highly Hydrogenated Free-Standing Graphene. *Nano Lett.* **2022**, *22* (7), 2971−2977.

(39) Dong, X.; Shi, Y.; Zhao, Y.; Chen, D.; Ye, J.; Yao, Y.; Gao, F.; Ni, Z.; Yu, T.; Shen, Z.; Huang, Y.; Chen, P.; Li, L.-J. Symmetry Breaking of Graphene Monolayers by Molecular Decoration. *Phys. Rev. Lett.* **2009**, *102* (13), No. 135501.

(40) Haberer, D.; Giusca, C. E.; Wang, Y.; Sachdev, H.; Fedorov, A. V.; Farjam, M.; Jafari, S. A.; Vyalikh, D. V.; Usachov, D.; Liu, X.; Treske, U.; Grobosch, M.; Vilkov, O.; Adamchuk, V. K.; Irle, S.; Silva, S. R. P.; Knupfer, M.; Büchner, B.; Grüneis, A. Evidence for a New Two-Dimensional C_4H-Type Polymer Based on Hydrogenated Graphene. *Adv. Mater.* **2011**, *23* (39), 4497−4503.

(41) Vishnyakova, E.; Chen, G.; Brinson, B. E.; Alemany, L. B.; Billups, W. E. Structural Studies of Hydrographenes. *Acc. Chem. Res.* **2017**, *50* (6), 1351−1358.

(42) Tjung, S. J.; Hollen, S. M.; Gambrel, G. A.; Santagata, N. M.; Johnston-Halperin, E.; Gupta, J. A. Crystalline Hydrogenation of Graphene by Scanning Tunneling Microscope Tip-Induced Field Dissociation of H2. *Carbon* **2017**, *124*, 97−104.

(43) Chen, H.; Bao, D.-L.; Wang, D.; Que, Y.; Xiao, W.; Qian, G.; Guo, H.; Sun, J.; Zhang, Y.-Y.; Du, S.; Pantelides, S. T.; Gao, H.-J. Fabrication of Millimeter-Scale, Single-Crystal One-Third-Hydrogenated Graphene with Anisotropic Electronic Properties. *Adv. Mater.* **2018**, *30* (32), No. 1801838.

(44) Kryachko, E. S. Intermolecular Interactions: Physical Picture, Computational Methods and Model Potentials. By Ilya G. Kaplan, John Wiley & Sons, Ltd, Chichester, England, 2006. ISBN-13:978−0−470−86332−9. *Int. J. Quantum Chem.* **2008**, *108* (1), 198−201.

(45) Blöchl, P. E. Projector Augmented-Wave Method. *Phys. Rev. B* **1994**, *50* (24), 17953−17979.

(46) Kresse, G.; Furthmüller, J. Efficiency of Ab-Initio Total Energy Calculations for Metals and Semiconductors Using a Plane-Wave Basis Set. *Comput. Mater. Sci.* **1996**, *6* (1), 15−50.

(47) Kresse, G.; Furthmüller, J. Efficient Iterative Schemes for Ab Initio Total-Energy Calculations Using a Plane-Wave Basis Set. *Phys. Rev. B* **1996**, *54* (16), No. 11169.

(48) Kresse, G.; Hafner, J. Ab Initio Molecular Dynamics for Liquid Metals. *Phys. Rev. B* **1993**, *47* (1), No. 558.

(49) Perdew, J. P.; Burke, K.; Ernzerhof, M. Generalized Gradient Approximation Made Simple. *Phys. Rev. Lett.* **1996**, *77* (18), No. 3865.

(50) Perdew, J. P.; Yue, W. Accurate and Simple Density Functional for the Electronic Exchange Energy: Generalized Gradient Approximation. *Phys. Rev. B* **1986**, *33* (12), No. 8800.

(51) Grimme, S.; Antony, J.; Ehrlich, S.; Krieg, H. A Consistent and Accurate Ab Initio Parametrization of Density Functional Dispersion Correction (DFT-D) for the 94 Elements H-Pu. *J. Chem. Phys.* **2010**, *132* (15), No. 154104.

(52) Maintz, S.; Deringer, V. L.; Tchougréeff, A. L.; Dronskowski, R. LOBSTER: A Tool to Extract Chemical Bonding from Plane-Wave Based DFT. *J. Comput. Chem.* **2016**, *37* (11), 1030−1035.